IBR Responses During a Real-World System-Wide Disturbance: Synchro-Waveform Data Analysis, Pattern Classification, and Engineering Implications

Hossein Mohsenzadeh-Yazdi, Chester (Chun) Li, and Hamed Mohsenian-Rad

***Abstract*—Time-synchronized waveform measurements, also known as synchro-waveforms, provide unprecedented insight into the complex behavior of inverter-based resources (IBRs) during system-wide disturbances. In this paper, synchro-waveforms from 68 solar and wind IBRs are analyzed during a 500 kV fault. Through feature extraction and pattern classification, the IBR responses are categorized into several distinct classes, including tripping during or after the fault, ride-through with a transient increase or decrease in current, prolonged current increases, and oscillatory responses. The characteristics of these responses are analyzed, and methods are proposed to convert the results into actionable information for operating IBR-rich networks.**

***Keywords*: Inverter-based resources, synchro-waveforms, dynamic response, classification, signal envelope, oscillations.**

I. Introduction

With the increasing penetration of inverter-based resources (IBRs), power systems are becoming more complex and dynamic. The North American Electric Reliability Corporation (NERC) has reported several system-wide incidents caused by the unexpected dynamic responses of IBRs to *transient disturbances* [1]. Understanding the behavior of IBRs during such disturbances requires access to synchro-waveforms [2][3] or other similar high-resolution waveform measurements [4].

In this paper, we analyze real-world synchro-waveform data from 68 IBRs during a 500 kV fault in Ontario, Canada. The sensor devices are Schneider's ION power quality meters [5]. The measurements have a resolution of 128 samples per cycle. The locations of the IBRs and the fault are shown in Fig. 1. For each IBR, the color denotes the class of the IBR's waveform response, as we will discuss in Section II-B.

The analysis in this paper is challenging due to various real-world difficulties. A major fault in a 500 kV power line is a rare but highly impactful event. Such a *rare occurrence* causes data scarcity, which poses a significant challenge for data-driven methods: we must train the models with very limited data. Furthermore, in real-world measurements, the distinctions among response classes are not always well-defined. Some IBRs exhibit characteristics that overlap multiple classes. Data quality is another challenge that further complicates the analysis. The proposed method effectively overcomes these various challenges and provides reliable response classification results with important practical implications.

II. Pattern Classification in IBR Responses

When a major fault happens, it triggers voltage disturbances across the network. This causes a *response* in each IBR's current. In this section, we classify the patterns in the *waveform signatures* in the *current response* of the IBRs. All the raw data that was used for the study in is paper is available at [6].

H. M. Yazdi and H. Mohsenian-Rad (Corresponding Author) are with UC Riverside, USA. C. Li is with Hydro One (Utility), Toronto, Canada.

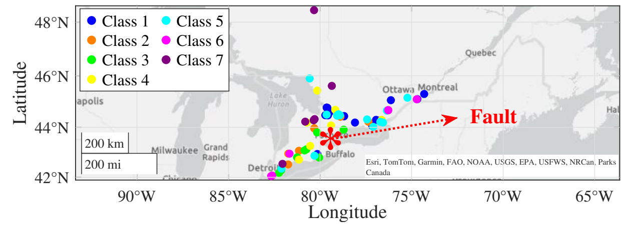

Fig. 1. All IBR locations and the location of the fault. The colors represent different classes of waveform patterns in the IBRs' responses to the fault.

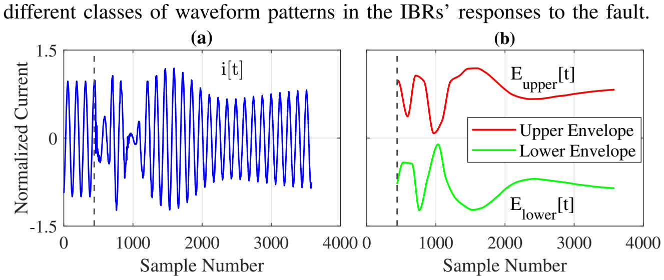

Fig. 2. (a) Normalized current waveform; (b) Upper and lower envelopes.

A. Feature Extraction and Classification Method

Due to the various sizes of the IBRs, we first normalize the injected current at each IBR based on its maximum *before* the fault. The normalized current waveform is denoted by $i[t]$.

After examining several features of $i[t]$ in time, frequency, and time-frequency domains, we concluded that the 'envelopes' of $i[t]$ can serve as effective features for our analysis. An example is shown in Fig. 2, where $E_{\text{upper}}[t]$ and $E_{\text{lower}}[t]$ denote the *upper-envelope* and *lower-envelope*, respectively. $E_{\text{upper}}[t]$ and $E_{\text{lower}}[t]$ are obtained by applying the Piecewise Cubic Hermite Interpolating Polynomial (PCHIP) method [7] to all local *maxima* and all local *minima* in $i[t]$, respectively.

Let $E^j_{\text{upper}}[t]$ and $E^j_{\text{lower}}[t]$ denote the envelopes at IBR j. Let $E^k_{\text{upper}}[t]$ and $E^k_{\text{lower}}[t]$ denote the envelopes at IBR k. Since the waveform measurements are *time-synchronized*, we can compare the waveform signatures of the IBR responses at IBRs j and k by using the following Euclidean distances:

$$\begin{aligned} D^{jk}_{\text{upper}} &= \|E^j_{\text{upper}}[t] - E^k_{\text{upper}}[t]\|_2, \\ D^{jk}_{\text{lower}} &= \|E^j_{\text{lower}}[t] - E^k_{\text{lower}}[t]\|_2. \end{aligned} \tag{1}$$

If the length of $i[t]$ from IBR i and IBR j is not the same, then we use the shorter length to calculate D^{jk}_{upper} and D^{jk}_{lower}. Due to occasional missing data on Phases A and B, only the data on Phase C are used for distance calculation and classification.

Next, we introduce another feature to compare the pre-event and post-event conditions in the current waveform measurements. Recall that the event-triggered waveform measurements

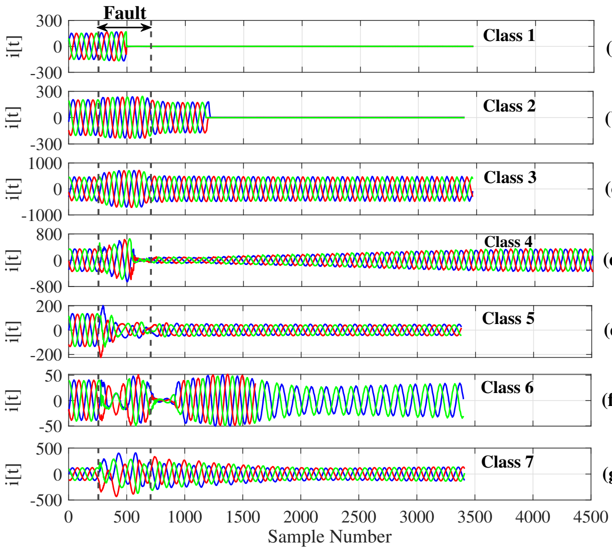

Fig. 3. Example of Current waveforms for the IBR response in each class.

contain several cycles, from a few cycles before the event to a few cycles after the event [8, p. 147]. Accordingly, we can compare the characteristics of the *first* cycle of the recorded current waveform, denoted by $i_{\text{first}}[t]$, with the *last* cycle of the recorded current waveform, denoted by $i_{\text{last}}[t]$. This comparison allows for the extraction of two critical ratios in the response of the IBR, namely the Fundamental Magnitude Ratio Γ and the Total Harmonic Distortion Ratio Λ:

$$\Gamma = \left|\text{FFT}\{i_{\text{first}}[t]\}\right| \,/\, \left|\text{FFT}\{i_{\text{last}}[t]\}\right|, \tag{2}$$

$$\Lambda = \text{THD}\{i_{\text{last}}[t]\} \,/\, \text{THD}\{i_{\text{first}}[t]\}, \tag{3}$$

where $|\cdot|$ denotes the magnitude, FFT$\{\cdot\}$ is the Fast Fourier Transform at fundamental frequency, and THD$\{\cdot\}$ is the Total Harmonic Distortion (THD); e.g., see its definition in [8, p. 142]. Notice the *reversed order* of the fractions in (2) and (3).

Accordingly, we define the new feature as:

$$F = \max\{\Gamma, \Lambda\}. \tag{4}$$

If Γ is *large*, then the event has caused a significant drop in the magnitude of the fundamental component of the IBR's current waveform. If Λ is *large*, then the event has caused a significant increase in the distortions of the IBR's current waveform. *In either case*, the event has caused a *significant disruption* in the IBR's operation. Thus, F can indicate *how severely* the event may have disrupted the IBR's operation. We propose using F as an *additional* feature, alongside D_{upper} and D_{lower}.

We may add that Γ and Λ are related to each other through:

$$\Lambda = \Gamma \sqrt{\frac{\text{RMS}\{i_{\text{last}}[t]\}^2 - \left|\text{FFT}\{i_{\text{last}}[t]\}\right|^2}{\text{RMS}\{i_{\text{first}}[t]\}^2 - \left|\text{FFT}\{i_{\text{first}}[t]\}\right|^2}}, \tag{5}$$

where RMS$\{\cdot\}$ is the Root Mean Square (RMS) value. The above equation is derived from the following standard equation: THD$\{\cdot\} = \sqrt{(\text{RMS}\{\cdot\}/\text{FFT}\{\cdot\})^2 - 1}$; see [8, p. 142].

Let $\mathcal{N}$ be the set of all IBRs, and $\mathcal{N}_{\text{train}}$ be the set of all IBRs whose waveform measurements are used as training data. For each IBR $j \in \mathcal{N}$, we define the vector of features as follows:

$$\mathbf{x}_j = [\ D^{jk}_{\text{upper}}\ ;\ D^{jk}_{\text{lower}}\ ; F^j\ ],\ \forall k \in \mathcal{N}_{\text{train}}. \tag{6}$$

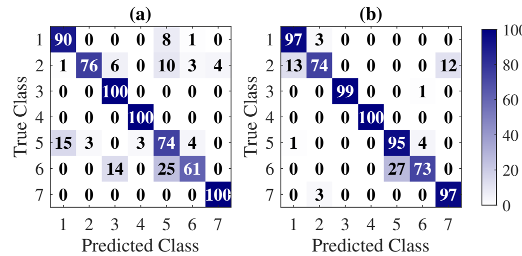

Fig. 4. Confusion matrices, where the features are: (a) D_{upper} and D_{lower}, yielding 85% accuracy; and (b) D_{upper}, D_{lower}, and F, yielding 92% accuracy.

The features in (6) depend on the training dataset. Each choice of the training data results in a different classification model.

Next, we use the One-vs-Rest (OvR) classification strategy based on Support Vector Machine (SVM) to train the classification model [9]. Let C denote the number of classes. In OvR, we develop a distinct hyperplane in the feature space over feature vector $\mathbf{x}$ that separates one class from the rest of the classes. Accordingly, we derive a total of C hyper-planes.

For each class $c = 1, \ldots, C$, the hyperplane is obtained as:

$$\text{Class } c \text{ Hyperplane:} \quad f_c(\mathbf{x}) = \mathbf{w}_c^T \mathbf{x} + b_c = 0, \tag{7}$$

where the parameters $\mathbf{w}_c$ and b_c are obtained by using regression with soft margins. In standard SVM, to see whether IBR j is in Class c, we check whether $f_c(\mathbf{x}_j) \geq 0$ or $f_c(\mathbf{x}_j) < 0$. However, since we use OvR with C hyperplanes, we define:

$$c^\star = \underset{c \in \{1,\ldots,C\}}{\arg\max}\ f_c(\mathbf{x}). \tag{8}$$

This ensures that exactly one class is selected for each IBR.

B. Classification Results

We identified $C = 7$ different classes of IBR responses. The number of cases in each class is as follows, adding up to a total of 68 cases for a total of 68 IBRs: 16 cases in Class 1; 9 cases in Class 2; 9 cases in Class 3; 7 cases in Class 4; 15 cases in Class 5; 6 cases in Class 6; and 6 cases in Class 7.

An example waveform response for each class is shown in Fig. 3. In Class 1, the IBR trips *during* the fault. In Class 2, the IBR trips *after* the fault is cleared. In Class 3, the IBR *rides through* the fault, supplying some fault current. In Class 4, the IBR exhibits a *short-lasting* (momentary) reduction in power injection. In Class 5, it exhibits a *long-lasting* reduction in power injection. In Class 6, it experiences *sub-synchronous* oscillations. In Class 7, the IBR exhibits *prolonged high current* for several cycles *after* the fault is cleared.

Fig. 4(a) shows the confusion matrix when the features are D_{upper} and D_{lower}. Fig. 4(b) shows the confusion matrix when the features are not only D_{upper} and D_{lower} but also F. The results are based on 1,000 random scenarios. In each scenario, 80% of the responses in each class are randomly selected for training, and the remaining 20% are used for testing.

Both confusion matrices show acceptable accuracy, with an overall accuracy of 85% in Fig. 4(a) and 92% in Fig. 4(b). The additional feature F is particularly helpful in improving the relatively lower accuracy in Classes 5 and 6 by distinguishing them from Classes 1 and 2. The operation of the IBRs in Classes 5 and 6 is not as significantly disrupted as that of the IBRs in Classes 1 and 2. This distinction is captured in F.

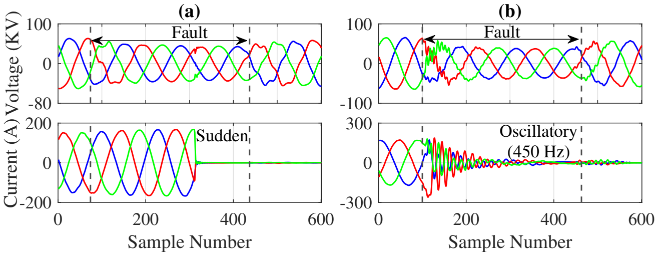

Fig. 5. Sudden versus oscillatory tripping in the IBR responses in Class 1.

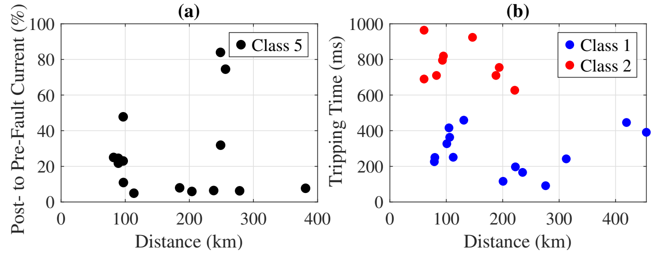

Fig. 6. Scatter plots: (a) post-to-pre-fault current ratio versus distance from the fault location; and (b) tripping time versus distance from the fault location.

Recall from Section I that there are several challenges in conducting the above IBR response classification, including data scarcity, overlapping characteristics among classes, and data quality. As a result, most data-driven methods cannot tackle this problem. For example, when we applied a classification method based on a Convolutional Neural Network (CNN), the overall accuracy was only 78%, significantly lower than the 92% accuracy achieved using our proposed method.

III. Further Discussions

1) High-Frequency Oscillations: Three IBRs, all in Class 1, experienced such oscillations during the fault. Fig. 5 compares two IBR responses in Class 1, one *without* oscillations in Fig. 5(a), and one *with* oscillations in Fig. 5(b). The frequency of the oscillations in current is 450 Hz (identical on all phases). There are also transient oscillations in voltage, at 700 Hz (Phase A), 960 Hz (Phase B), and 850 Hz (Phase C).

2) Sub-synchronous Oscillations: Six IBRs, all in Class 6, experienced sub-synchronous oscillations, i.e., at frequencies *below* the fundamental frequency. The available data are sufficient to detect the presence of sub-synchronous oscillations. However, it is not sufficient to fully characterize them. This is because some WMUs record only a few cycles after the disturbance. Due to the low frequency of sub-synchronous oscillations, we need waveform data over longer periods.

3) Partial Tripping in IBRs with Multiple Inverters: The IBRs in Class 5 had a long-lasting reduction in power injection. The utility records revealed that all IBRs in this class have multiple inverters and they experienced *partial tripping*, where a *subset* of inverters tripped. Tripped inverters had Class 1 or Class 2 responses. Inverters that did not trip had Class 3 responses. However, since the waveform measurements are collected at each IBR's interconnection point, the *overall* response is in Class 5. The ratio of tripped inverters is estimated by examining the ratio of post-fault current to pre-fault current, as shown in Fig. 6(a). It varies from 5% to 84%.

4) Timing and Distance: Both Class 1 and Class 2 involve tripping. Fig. 6(b) shows the scatter plot of the tripping time (from the start of the fault) versus the distance from the fault. We can see that the timing of tripping significantly varies even within the same class. The IBRs in Class 1 are between 78 km to 455 km away from the location of the fault. However, the farthest IBR in Class 2 is 220 km from the fault, which is less than half of the farthest IBR in Class 1.

5) Causes of Post-Fault Tripping: IBRs in Class 2 trip *after* the fault is cleared. The circumstances of a post-fault tripping are revealed by analyzing the voltage and current waveform measurements. An example is shown in Fig. 7. In Fig. 7(a), the IBR trips four cycles after the fault is cleared. After zooming in, Fig. 7(b) shows the exact moment when the IBR trips. Notice the voltage distortion at the moment of tripping.

6) Geographical Patterns: Recall that the colors on the map in Fig. 1 denote the classes of the IBRs. Some geographical patterns can be identified in this figure. Almost all IBRs in Class 1 are on the North and North-east side of the fault location. Almost all IBRs in Class 3 are on the West side of the fault location. Almost all IBRs in Class 7 are on the North side of the fault. The IBRs in Classes 2, 4, 5, and 6 are geographically scattered across the region with no pattern.

7) Type of Resource: Almost all IBRs in Classes 1 and 5 are solar. The rest of the classes include both solar and wind IBRs. Classes 2 and 7 have more wind than solar IBRs. Classes 3, 4, and 6 have more solar than wind IBRs. Class 7 maintains a high current even after the fault is cleared. This is likely due to internal dynamics in the IBRs in this class. All other classes stop supplying fault current once the fault is cleared.

IV. Method to Assist System Operation

The results from IBR response classification can help transmission and distribution operators address some of the challenges in IBR-rich networks. According to the recent NERC recommendations [1], it is crucial for system operators to identify and mitigate IBRs with *abnormal performance*. However, pinpointing such IBRs, especially in a timely and automated manner, remains a significant challenge. In this section, we propose a methodology to address this open problem.

For each IBR i, let A_i denote the set of all other IBRs of the same type. For example, if IBR i is a solar (wind) unit, then A_i consists of all other solar (wind) units. Next, we apply a two-stage ranking filter to set A_i to define:

$$S_i = \text{Top}-M\big\{\text{Top}-N\big(A_i, \text{Closest Distance to } i\big), \text{Closest Voltage Level to } i\big\}. \quad (9)$$

where M and N are two integer parameters satisfying $M \leq N$. Here, S_i contains the M IBRs with the closest voltage levels to IBR i among the N nearest IBRs of the same type. The IBRs in set S_i are, in essence, *comparable* to IBR i. Parameters M and N do not necessarily need to be the same for all IBRs. Grid operators may choose M and N differently for each IBR based on their knowledge of comparable IBRs.

To identify *abnormal performance*, we use set S_i to define:

$$\rho_i = (1/M) \textstyle\sum_{j \in S_i} 1\big(\text{Class}\{\text{IBR } i\} = \text{Class}\{\text{IBR } j\}\big) \quad (10)$$

as the fraction of the IBRs in set S_i that have the same class as IBR i, where $1(\cdot)$ is the 0-1 indicator function. If ρ_i is low,

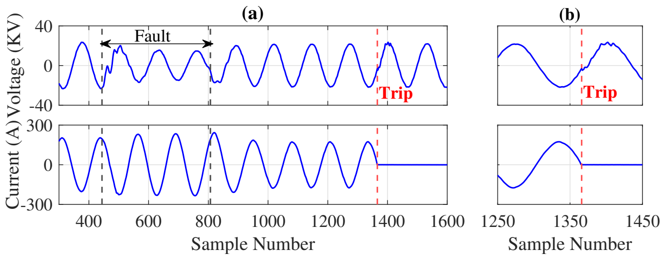

Fig. 7. Examining the circumstances of a post-fault tripping by zooming in at the waveform measurements at an IBR in Class 2.

then the behavior of IBR i was considerably different from the IBRs that are comparable to IBR i. This can be used to flag IBR i to *potentially* have abnormal performance.

As an example, consider IBR $i = 6$. Its response is Class 1, which indicates tripping during the fault. If we set $N = 10$ and $M = 5$, we can obtain: $S_6 = \{1, 5, 61, 64, 67\}$, where the Classes are 2, 5, 3, 4, 4, respectively. We have: $\rho_6 = 0$; because no IBR in set S_6 is in the same class as IBR 6, i.e., no IBR in set S_6 trips during the fault. Thus, IBR 6 can be flagged for potential abnormal performance (abnormal tripping).

As another example, consider IBR $i = 45$. Its response is again Class 1, i.e., tripping during the fault. We have: $S_{45} = \{47, 49, 54, 55, 56\}$, where the Classes are 1, 1, 1, 5, 1, respectively. We have: $\rho_{45} = 4/5 = 0.8$. Accordingly, IBR 10 is likely *not* an IBR with abnormal behavior because the majority of the other comparable IBRs also demonstrated a similar behavior, i.e., they too tripped during the fault.

The IBRs that are flagged as potentially abnormal may trigger further investigation by the transmission or distribution operator in collaboration with the site owner/operator.

V. Conclusions

Using real-world synchro-waveform data, we analyzed the responses of several IBRs to a system-wide disturbance. Our analysis included: (a) introducing and extracting features from waveform signatures; (b) classifying and characterizing diverse patterns in IBR responses; and (c) discussing the key take-aways and implications. The practical findings of this study can help utilities enhance situational awareness and predict the dynamic behavior of IBRs during system-wide disturbances, to improve the stability and reliability of their networks.

References

[1] North American Electric Reliability Corporation, "Odessa disturbance texas events: May 9 and june 26, 2021," NERC, Tech. Rep., 2021.
[2] H. M. Rad and W. Xu, "Synchro-waveforms: A window to the future of power systems data analytics," *IEEE Power and Energy Magazine*, 2023.
[3] M. Izadi and H. Mohsenian-Rad, "Characterizing synchronized lissajous curves to scrutinize power distribution synchro-waveform measurements," *IEEE Trans. on Power Systems*, vol. 36, pp. 4880–4883, 2021.
[4] Z.-J. Ye and H. Mohsenian-Rad, "Transforming conventional waveform measurements into synchro-waveforms: A data-driven method for event signature alignment and synchronization operator estimation," *IEEE Trans. on Smart Grid*, vol. 16, pp. 1495–1509, 2025.
[5] S. Electric. [Online]. Available: https://www.se.com/ww/en/
[6] https://ieee-synchrowaveform.engr.ucr.edu/data-sets.
[7] https://www.mathworks.com/help/matlab/ref/pchip.html.
[8] H. Mohsenian-Rad, *Smart grid sensors: Principles and applications*. Cambridge University Press, 2022.
[9] J. Xu, "An extended one-versus-rest support vector machine for multi-label classification," *Neurocomputing*, vol. 74, pp. 3114–3124, 2011.